# **Journal Name**

# **ARTICLE TYPE**

Cite this: DOI: 00.0000/xxxxxxxxxx

# Elucidating Correlated Defects in Metal Organic Frameworks Using Theory-Guided Inelastic Neutron Scattering Spectroscopy<sup>†</sup>

Lucas S. R. Cavalcante,\*a Makena A. Dettmann,a Tyler Sours,a Dong Yang,a Luke L. Daemen,b Bruce C. Gates,a Ambarish R. Kulkarni,\*a and Adam J. Moulé\*a

Received Date Accepted Date

DOI: 00.0000/xxxxxxxxxx

Metal Organic Frameworks (MOFs) that incorporate metal oxide cluster nodes, exemplified by UiO-66, have been widely studied, especially in terms of their deviations from the ideal, defect-free crystalline structures. While defects such as missing linkers, missing nodes, and the presence of adventitious synthesis-derived node ligands (such as acetates and formates) have been proposed, their exact structure remains unknown. Previously, it was demonstrated that defects are correlated and span multiple unit cells. The highly specialized techniques used in these studies are not easily applicable to other MOFs. Thus, there is a need to develop new experimental and computational approaches to understand the structure and properties of defects in a wider variety of MOFs. Here, we show how low-frequency phonon modes measured by inelastic neutron scattering (INS) spectroscopy can be combined with density functional theory (DFT) simulations to provide unprecedented insights into the defect structure of UiO-66. We are able to identify and assign peaks in the fingerprint region (< 100 cm<sup>-1</sup>) which correspond to phonon modes only present in certain defective topologies. Specifically, this analysis suggests that our sample of UiO-66 consists of predominantly defect-free fcu regions with smaller domains corresponding to a defective bcu topology with 4 and 2 acetate ligands bound to the  $Zr_6O_8$  nodes. Importantly, the INS/DFT approach provides detailed structural insights (e.g., relative positions and number of acetate ligands) that are not accessible with microscopy-based techniques. The quantitative agreement between DFT simulations and the experimental INS spectrum combined with the relative simplicity of sample preparation, suggests that this methodology may become part of the standard and preferred protocol for the characterization of MOFs, and in

# 1 Introduction

As investigations of metal–organic frameworks (MOFs) have developed beyond synthesis, discovery, and bulk structure determination, researchers have increasingly focused on novel applications such as removal of water <sup>1</sup> and of CO<sub>2</sub> <sup>2</sup> from air. These potentially disruptive technologies require the MOF to be sufficiently stable under ambient conditions. MOF stability depends on the prevalence of structural defects and imperfections in the underlying structure <sup>3</sup>. Defects include missing linkers and nodes and the presence of adventitious node ligands that arise during the synthesis. Defects have thus become central topics in MOF science; the associated challenges and opportunities have been recently reviewed. Fang et al. <sup>4</sup>, Sholl and Lively <sup>5</sup>, Dissegna et al. <sup>6</sup>, Feng et al. <sup>7</sup>, Ma et al. <sup>8</sup>

Although several studies have leveraged *defect engineering* in improving the catalytic and separation properties of MOFs, the role of defects on other properties (e.g., energy storage,  $^{9,10}$  water purification,  $^{11}$  supercapacitors,  $^{12}$  electrocatalysis,  $^{13,14}$  mechanical properties,  $^{15-17}$  conductivity,  $^{18-21}$  optical properties  $^{8,22,23}$ ) is not well understood. Additionally, although we focus on porous MOF materials, we anticipate that defects play an important role in related materials such as dense -MOFs  $^{24-26}$  and porous organic cages  $^{27}$ 

More specifically to the subject of this work, defects in UiO-66 MOFs are of great interest because they can act as catalytically active sites <sup>28,29</sup> or as catalyst supports for other metal complexes <sup>30,31</sup>. Investigations of the synthesis chemistry of MOFs such as UiO-66 provide insight into the control of defects. <sup>32</sup> The elucidation of the defect chemistry of MOFs is progressing using combined characterization techniques. Combined use of diffuse x-ray scattering, electron microscopy, and anomalous X-ray diffraction (XRD) demonstrated correlations between defects

particular, for elucidating the structure defects in these materials.

Department of Chemical Engineering, University of California, Davis, CA, 95616, USA
Neutron Scattering Division, Oak Ridge National Laboratory, Oak Ridge, Tennessee

<sup>\*</sup> Neutron Scattering Division, Oak Riage National Laboratory, Oak Riage, Tennesse 37831, United States

<sup>†</sup> Electronic Supplementary Information (ESI) available. See DOI: 00.0000/00000000.

in a UiO-66 (Hf) MOF and phase separation between defective and defect free regions on the nanoscale in hafnium-containing metal oxide cluster nodes.  $^{33}$  High-resolution transmission electron microscopy (TEM) images have shown the evolution of defect distributions as function of MOF crystallization time.  $^{34}$  Indirect characterization methods including thermogravimetric analysis  $^{35}$ , acid-base titration  $^{36}$ , nitrogen adsorption  $^{3}$ , and analysis of the products of MOFs digested in NaOH in  $\rm D_2O$  by  $^{1}H$  NMR spectroscopy  $^{37}$  also enable quantification of defect chemistry and density, but cannot co-locate the chemical species with the physical structure. Table 1 summarizes the advantages and disadvantages of the mentioned techniques for characterizing defects in MOFs.

In spite of these excellent characterization options, progress in relating MOF structure and chemistry to materials properties like catalytic activity and structural/chemical stability is limited by the lack of characterization techniques that provide atomiclevel structural details. Here, we combine density functional theory (DFT) simulations with inelastic neutron scattering (INS) data to develop a general approach for spectroscopically characterizing defects in MOFs. We quantify the dynamics of missing linker defects and adventitious ligands in MOF UiO-66 using the low-frequency vibrational modes ( $< 100 \text{ cm}^{-1}$ ), measured by INS. Then we create an ensemble of possible defect configurations (e.g., the density and positions of missing linkers) in various topologies (e.g., fcu, bcu, reo, scu) with DFT. Quantitative comparison between the measured and simulated spectra is used to fingerprint the exact positions, density, and chemistry of missing linkers defects and adventitious node ligands.

INS is effective for investigating structure and dynamic disorder in a wide range of materials. 38-40 While INS has been used to investigate gas adsorption and phase changes in MOFs<sup>41,42</sup>, this technique has not been used to elucidate the structure of defects in these materials. INS is ideally suited to address the challenge of defect structure because, in contrast to XRD (which probes the structures of crystalline domains), INS is a quantitative spectroscopic technique that probes the dynamics of the whole sample. Unlike optical vibrational spectroscopies (e.g., Raman and infrared) that measure the energy exchanged by scattered photons which obey selection rules, INS is not limited by photon selection rules since it measures the exchanged energy of neutrons scattered by the atomic nuclei. Also, INS samples the complete Brillouin zone, not just the gamma point as for the optical spectroscopies, enabling resolution of phonons that cannot be detected using optical spectroscopies. In the SI, we present a spectra comparison between optical spectroscopy methods (Raman and infrared) and INS, so the differences are made clear to the reader 43. Finally, owing to the high neutron scattering cross-section of the <sup>1</sup>H nucleus, INS is particularly sensitive to the molecular environment of organic linkers and node ligands. Because the <sup>1</sup>H atoms are pendant molecules to the structural organic backbone, they are remarkably sensitive to subtle changes in the intermolecular environment.

We now illustrate the value of INS for structural characterization of UiO-66 samples that have been synthesized using modulators to incorporate node formate, acetate, and trifluoroacetate

ligands. The extensive literature of UiO-66 provides a foundation for placing the new results in a broad context. 3,7,32,34,35,37,44-52 Since INS probes all the coupled vibrational modes involving hydrogen atoms, the interpretation of INS spectra is computationally challenging. Detailed modeling of the phonon modes (typically done with DFT) is necessary to link experimentally observed peak positions and intensities with specific vibrational modes. The high costs of the DFT calculations have, for the most part, limited this approach to simple crystalline materials with high structural symmetry (including a few nearly defect-free MOFs). 53,54 For example, Deacon et al. 42 combined DFT calculations with INS spectra to show the pressure-induced phase transition of ZIF-L to ZIF-8. Because defects in MOFs reduce the overall symmetry of the structure, INS simulations of defective MOFs require larger simulation volumes and are orders of magnitude more computationally expensive than those of their pristine analogs.

To work toward overcoming these limitations, we developed a Python-based workflow (denoted as DCS-Flow <sup>55</sup>) that facilitates seamless integration between the separate components of an INS simulation. DCS-Flow is an accurate, reproducible, efficient workflow for calculating phonon modes and the INS spectrum using DFT. The flowchart in Figure S1 in the Supporting Information summarizes our approach, which allows comparisons of experimental spectra with predictions from a library of candidate defect structures. We now illustrate the method by comparing predicted spectra with INS data characterizing UiO-66 with various node ligands. The results provide unprecedented insights into the structure of the missing linker defects and the ligands that reside on the Zr-nodes. We posit that this integrated experiment-theory approach can be broadly extended to a wide family of MOFs.

# 2 Results and discussion

The structure of defect-free UiO-66 includes Zr<sub>6</sub>O<sub>8</sub> nodes that are interconnected to form a fcu topology, where each node is bound to 12 linkers. The average connectivity of the nodes is controlled during synthesis by the use of modulators (e.g., acetic acid), which form anions that compete with the linker precursor anions during synthesis. For example, use of acetic acid (AA) as the modulator (with a modulator to ZrCl4 mol ratio of 30) resulted a UiO-66 sample with 10.9(4) linkers/node (i.e., 1.0(6) missing linkers/node) where the number in parentheses is the numerical value of the standard uncertainty. We denote this material as UiO-66-AA. When trifluoroacetic acid (TFA) was used as a modulator instead of acetic acid, with the same modulator to ZrCl<sub>4</sub> ratio, the pKa of the synthesis solution was lower, the crystallization time was reduced, and the resulting MOF had 3.52 missing linkers per node. The experimental characterization (IR Spectroscopy, Powder X-ray Diffraction, Scanning Electron Microscopy, Transmission Electron Microscopy, Brunauer-Emmett-Teller (BET) Surface Area, Thermal Gravimetric Analysis, and <sup>1</sup>H NMR Spectroscopy) of the sample measured here was published previously. Wei et al. 37

The linkers/node ratio, derived from <sup>1</sup>H NMR Spectroscopy, does not determine the relative positions of the missing linkers in the MOFs. The interpretation of linker and defect structure

Methods	Advantages	Disadvantages
RAMAN/FTIR	Able to derive some local defects details	Not enough to characterize defect occu- pancy and define defect type
XRD	Able to derive crystal structure detecting missing clusters	No organic linker information (linker defects)
HRTEM	Detailed atomic observation of defects	Impractical to define/quantify all defects in the sample
Thermogravimetric analysis	Able to quantify defects	No atomic detail of the defects structure
Acid-base titration	Able to quantify defects and active site information	No definition of the defects type (cluster or linker) and positions
Nitrogen adsorption	Indicate defects existence	No information on the definition/quantification of defects
<sup>1</sup> H NMR	Robust quantification of modulator species and linkers	No atomic detail of the defects structure
INS	Provide atomic-level structural/chemical details of the defects	Semiquantitative assessment of defects

Table 1 Defect characterization methods summary

from the molar ratio is further complicated by the presence of other less-coordinated topologies in the UiO-66 samples. 33

All the experiments were done at 5 K since the dynamics of the system can strongly suppress all neutron intensities. This can be confirmed by the Debye-Waller factor, a exponential temperature dependent term present in the scattering law which is used to model all modern neutron spectroscopy data. Therefore, INS measurements are generally done at low temperatures. Otherwise, a room temperature spectrum is almost the same for any organic compound 40.

# 2.1 Simulating defect free topologies

The main goal of this work is to develop an atomic-scale picture of the defects structure. An appropriate starting point to understanding defects in UiO-66 topologies is to simulate defect free and under-coordinated structures, shown in Figure 1a. 34 These under-coordinated topologies include varying numbers of missing linkers per node. The sites on the nodes where linkers are missing in UiO-66 are often occupied by adventitious ligands, including acetate derived from the acetic acid modulator and formate derived from DMF. 34 For example, the bcu topology presents the same density of  $Zr_6O_8$  nodes as fcu (1 node / unit cell), but has 8 linkers per node instead of 12 linkers per node; thus there are four sites on each node that might either be capped by a proton or occupied by adventitious ligands. The reo and scu topologies have lower node densities per unit cell, meaning a more open MOF framework. The reo topology incorporates 8 linkers/node. The scu topology is more complex, with either 8 or 4 linkers/node. Figure 1b presents the simulated INS spectra of defect-free fcu, and defected bcu, reo, and scu topologies where the linker-occupied sites in the less-coordinated topologies (bcu, scu, and reo) are occupied by formate ligands derived from the DMF solvent. The simulation results are compared with the INS data for a UiO-66 sample synthesized with acetic acid modulator (i.e., UiO-66-AA).

While the INS spectra of the four topologies show some similar features, there is excellent agreement between experiment and the INS simulations for the fcu topology over the entire energy range. The simulated INS spectra for the other topologies are less consistent with the data, especially in the regions of 250 and  $1450 \text{ cm}^{-1}$ ; the peaks in these regions arise from the increased abundance of formate ligands in the under-coordinated topologies (details in Supporting Information). Two central conclusions emerge from this comparison:

- 1. our computational methods and the DCS-Flow approach are quantitatively accurate in predicting the vibrational modes and the resulting INS spectrum of UiO-66 over an energy range of 5-5000  $cm^{-1}$  (Fig. S2)
- 2. the defect-free fcu topology provides the best overall representation of the UiO-66-AA sample among those investigated (details on how the correlation was calculated were given in the SI).

Conclusion 2 is especially encouraging because the experimental UIO-66-AA sample contains only 1.0(6) missing linkers/node. <sup>37</sup> Fig. 1c shows a quantitative comparison between the experimental and simulated spectra from Fig. 1b. The fcu structure shows the highest correlation, followed by equally good correlations between the bcu and reo topologies and much poorer correlation with the scu structure. Assuming that the sample contains only pure fcu and bcu topologies that phase separate, then a sample with 1.0 missing linkers/node would be 75% fcu with no missing linkers and 25% bcu with 4.0 missing linkers/node.

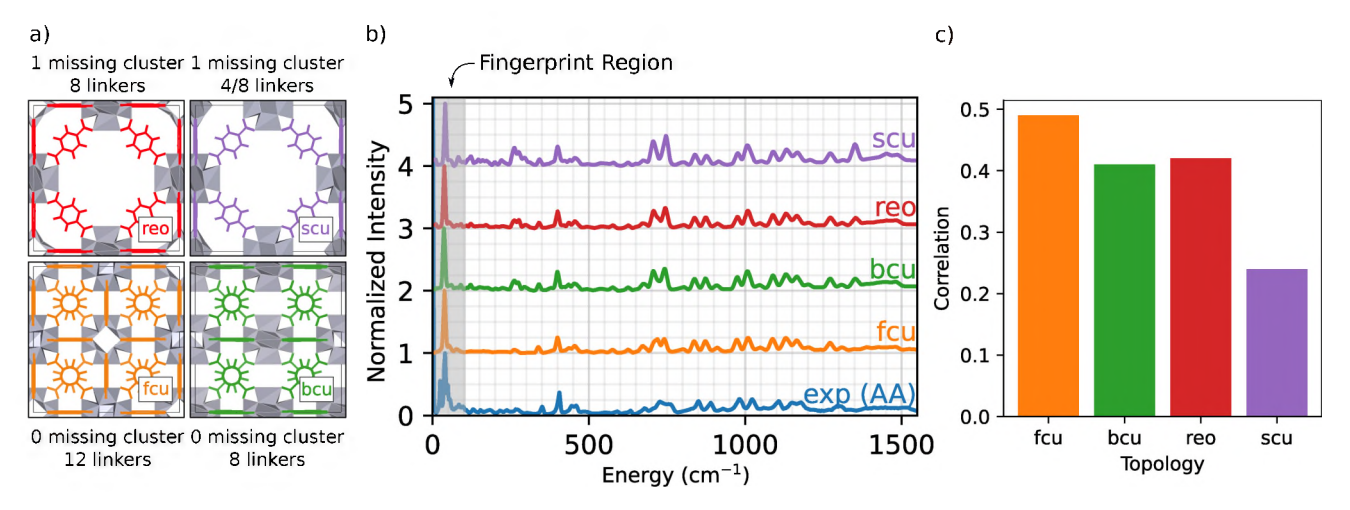


Fig. 1 (a) Four proposed UiO-66 topologies; gray geometries represent the node clusters and colored geometries the linkers. (b) Comparison of INS spectra of UiO-66 at wavenumbers up to 1550 cm<sup>-1</sup>. INS data of UiO-66-AA recorded at 5 K (blue curve) and DFT-simulated spectrum of the fcu (orange), bcu (green), reo (red), and scu (purple) topologies. The non-linker-occupied sites in the less-coordinated topologies (bcu, scu, and reo) are occupied by formate ligands. The gray shaded area in (b) denotes the INS fingerprint region (below 100 cm<sup>-1</sup>). (c) Correlation comparison between experimental INS spectrum of UiO-66-AA and DFT simulated spectra of chosen topologies.

We emphasize that the above analysis required a thorough testing of the parameters that are relevant for the INS simulation. Specifically, we evaluated the effect of DFT functionals, energy cutoffs, and mesh sampling of the phonon Brillouin zone to achieve optimal agreement with experiment, as reported previously <sup>38</sup>. We posit that such high-cost, high-quality simulations are necessary for direct comparison and correct interpretation of MOF INS experiments.

A fundamental advantage of INS over other vibrational spectroscopies is the high signal-to-noise ratio obtained at low wavenumbers (e.g.,  $<100~\rm cm^{-1}$ ). These low-frequency phonon modes are often associated with coupled motions (e.g., wagging, twisting, bending, rocking, breathing) that span several unit cells and involve multiple atoms in the structure. In the following sections, we demonstrate that this low-frequency INS data serves as a fingerprint region for identifying the type (e.g., AA, formate, TFA), density, and relative positions of linkers and adventitious ligands bound to the  $\rm Zr_6O_8$  node in UiO-66.

Figure 2 compares the experimental INS measurement for UIO-66-AA (blue) with the DFT simulations of the INS spectrum in the low-frequency fingerprint region. The experimental INS data for UiO-66-AA data are characterized by four key features:

- 1. a major peak (denoted  $T_L$ ) at about 40 cm<sup>-1</sup> with a small, red-shifted shoulder ( $\sim$ 35 cm<sup>-1</sup>)
- 2. a red-shifted double peak ( $\sim$ 25 cm<sup>-1</sup>, designated as A peak)
- 3. a blue-shifted double peak ( $\sim$ 50 cm<sup>-1</sup>, designated as B peak)
- 4. a broad shoulder at 55 cm<sup>-1</sup> (designated as C peak)

While the A, B, and C peaks are not observed in the simulations, all four topologies show a phonon mode close to  $T_L$  (i.e.,  $35 - 40 \text{ cm}^{-1}$  region). To identify the specific molecular vibration corresponding to this peak, we calculate the eigenvalues

and eigenvectors of the DFT-simulated dynamical matrix (determined using finite displacement, as implemented in Phonopy). <sup>56</sup> With this normal mode analysis approach, the eigenvalue for each phonon mode corresponds to the characteristic energy (i.e., the wavenumber), while the molecular motion itself is determined by the eigenvector (one vector for each atom in the system). Importantly, the eigenvectors are further analyzed to determine which atoms contribute to the phonon mode (e.g., node, linker, acetate ligand etc.)

The above analysis shows that the  $T_L$  peak originates from a back and forth rocking/twisting motion about the longitudinal axis of the linker (Figure 2b, see  $fcu\_40cm-1.gif$  animation in the SI). Since the phonon mode is dominated by linker motions (i.e.,  $Zr_6O_8$  nodes are not involved), it is observed at similar energies (and wavenumbers) across the different topologies. The slight differences in the position of the peak arise due to the small variations in the lattice constants for the four topologies. To the best of our knowledge, this is the first unambiguous assignment of a linker-specific phonon mode in the fingerprint region for any MOF. (The study by Deacon et al. was unable to identify modes below  $200 \text{ cm}^{-1}$ .  $^{42}$ )

We now explain the origin of A, B, and C peaks in the experimental INS. Since these features are not observed in the simulated INS spectra for any of the four topologies, we conclude that chemical defects due to the presence of adventitious synthesisderived node ligands in UiO-66-AA are responsible for the peaks A, B, and C. Further evidence for this conclusion comes from comparison between the UiO-66-AA (blue) and UiO-66-TFA (brown) spectra (Figure 2a). The spectrum of UiO-66-TFA lacks the A, B, and C peaks and the TFA synthesized sample does not contain any acetate groups. Thus, we associate these peaks with the presence of acetate ligands in the structure. This assignment is consistent with earlier work that methyl groups in ZIF-8 are associated with a 25 cm<sup>-1</sup> peak in the INS spectrum. <sup>57</sup> The computational models that consider only connectivity defects are incomplete and fail

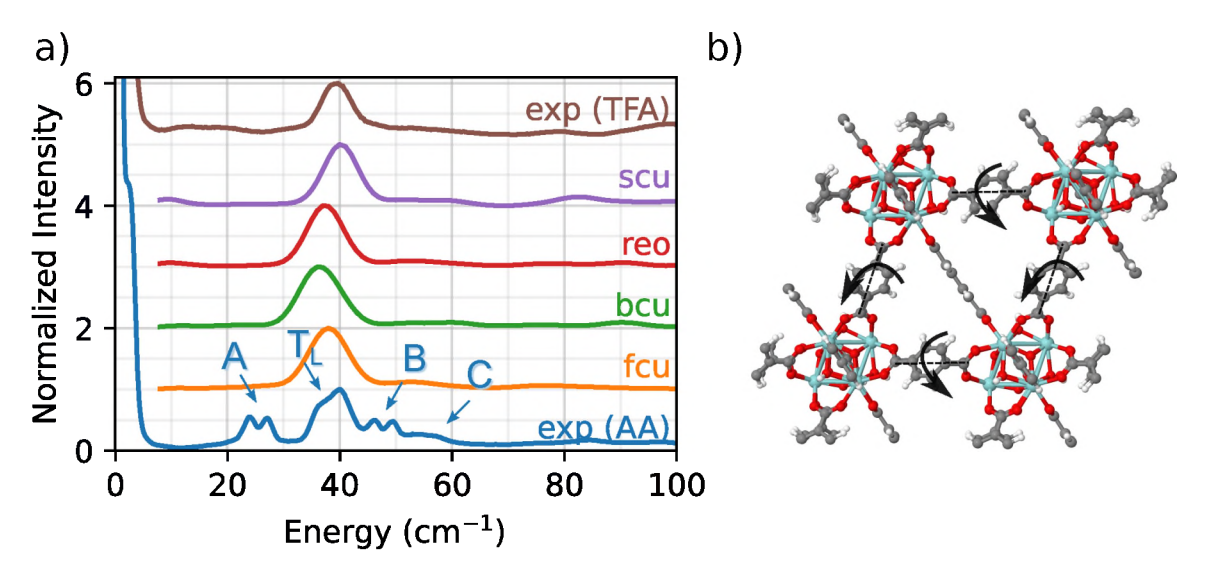


Fig. 2 (a) Fingerprint region: INS spectra at frequencies up to  $100 \text{ cm}^{-1}$  for all simulated topologies and comparison with experiment for samples made with acetic acid called UiO-66-AA (blue) and trifluoroacetic acid called UiO-66-TFA (brown) modulators. Experimental peaks that are missing from the simulations and from the experimental spectrum of the sample modulated with trifluoroacetic acid are denoted as follows: A, a doublet at about 25 cm<sup>-1</sup>; B, a doublet at about 45 cm<sup>-1</sup>; and C, a shoulder at about 55 cm<sup>-1</sup>. Because fluorine atoms have a low INS cross-section, peaks representing CF<sub>3</sub> dynamics are essentially missing from the INS spectrum, and the A, B, and C peaks are assigned to dynamics of the methyl groups of acetate ligands. (b) DFT-simulated vibrational mode corresponding to peak  $T_L$  is a rocking mode common to attached linkers in all topologies.

to capture the structural and chemical complexity of the experimental sample.

#### 2.2 Simulating acetic acid defects

To further investigate how the modulator acetic acid led to changes in the INS spectra, we created a library of UiO-66 models in which the formate ligands in the bcu, reo, and scu topologies were replaced with acetate ligands. This replacement resulted in a well-defined set of topologies with varying numbers of linkers and acetate ligands bonded to the nodes. In each of the three cases, the total coordination number of the node is 12.

A comparison of the predicted INS spectra of the three undercoordinated topologies with experiment is shown in Figure 3a. In contrast to the pristine fcu topology and the formate-containing bcu, reo, and scu topologies (Figure 2), we now observe many more peaks in the fingerprint region, indicative of the acetate ligands.

A central advantage of our DFT-based DCS-Flow approach is the ability it provides to computationally set the scattering cross-sections of individual atoms to zero. Thus, to isolate the vibrational modes that are related to these peaks, we set the cross-section of each atom except those of the acetate groups to zero. The resulting spectra in Figure 3b provides strong evidence that the low-energy doublets indeed originate from acetate groups bonded to the  $\rm Zr_6O_8$  clusters at defect sites.

The results show that the acetate group contributes differently to the INS spectrum depending on the topology, which means that the molecular environment around the acetate group strongly affects the correlated wag and twist motions of the methyl groups. Using bcu as an example (green in Fig. 3b), we observe two main features at 12 cm<sup>-1</sup> (a1) and at 16 cm<sup>-1</sup> (a2). This doublet corresponds to coupled twisting motions of two methyl groups (from

the acetate) on opposing sides of the  $\rm Zr_6O_8$  node in a diagonal fashion (see Figure 3c). There are two different peaks because there are two different symmetric arrangements of methyl groups on each node. These modes are localized only on the methyl groups of the acetate ligand. Neither the linker (which dominates the  $\rm T_L$  peak) or the  $\rm Zr_6O_8$  node are coupled to the doublet modes (see animations bcu-4A\_a1.gif and bcu-4A\_a2.gif in the SI).

In both the reo and scu cases, two different groups of acetate structures are involved in rocking motions that couple with the surrounding linkers. The coupling of the acetate motion with the linkers' motion increases the total energy of the mode. The scu simulated spectrum presents a stronger signal of peak C (Figure 3) because it contains a smaller number of linkers and a correspondingly larger number of acetate ligands.

This analysis shows that the A, B, and C peaks originate from the acetate defects and are associated with different phonon modes depending on the motions that are specific to the bonding environment in each topology. The slight disagreement in the peak positions ( $\sim 10~\rm cm^{-1}$ , 1.24 meV) of the bcu case is due to the fact that the INS simulations are performed using a 1x1x1 unit cell of the MOF, which corresponds to an infinite network of defective nodes. Nevertheless, our simulations provide strong evidence that the experimental A peaks arise from the coupled twisting of the methyl groups bound to the  $Zr_6O_8$  node of UiO-66-AA. The phonon modes corresponding to a1 (bcu-4A\_a1.gif) and a2 (bcu-4A\_a2.gif) are presented in the SI as movie files.

We showed, in Figure 1, that the simulated INS spectrum from a non-defective lattice provides the best fit to the UiO-66-AA spectrum. This assignment was expected considering that the NMR measurements show an average ratio of one missing linker per node. This would correspond to a 3:1 volume ratio of fcu:bcu or fcu:reo topologies. The analysis in Figure 3 makes a strong

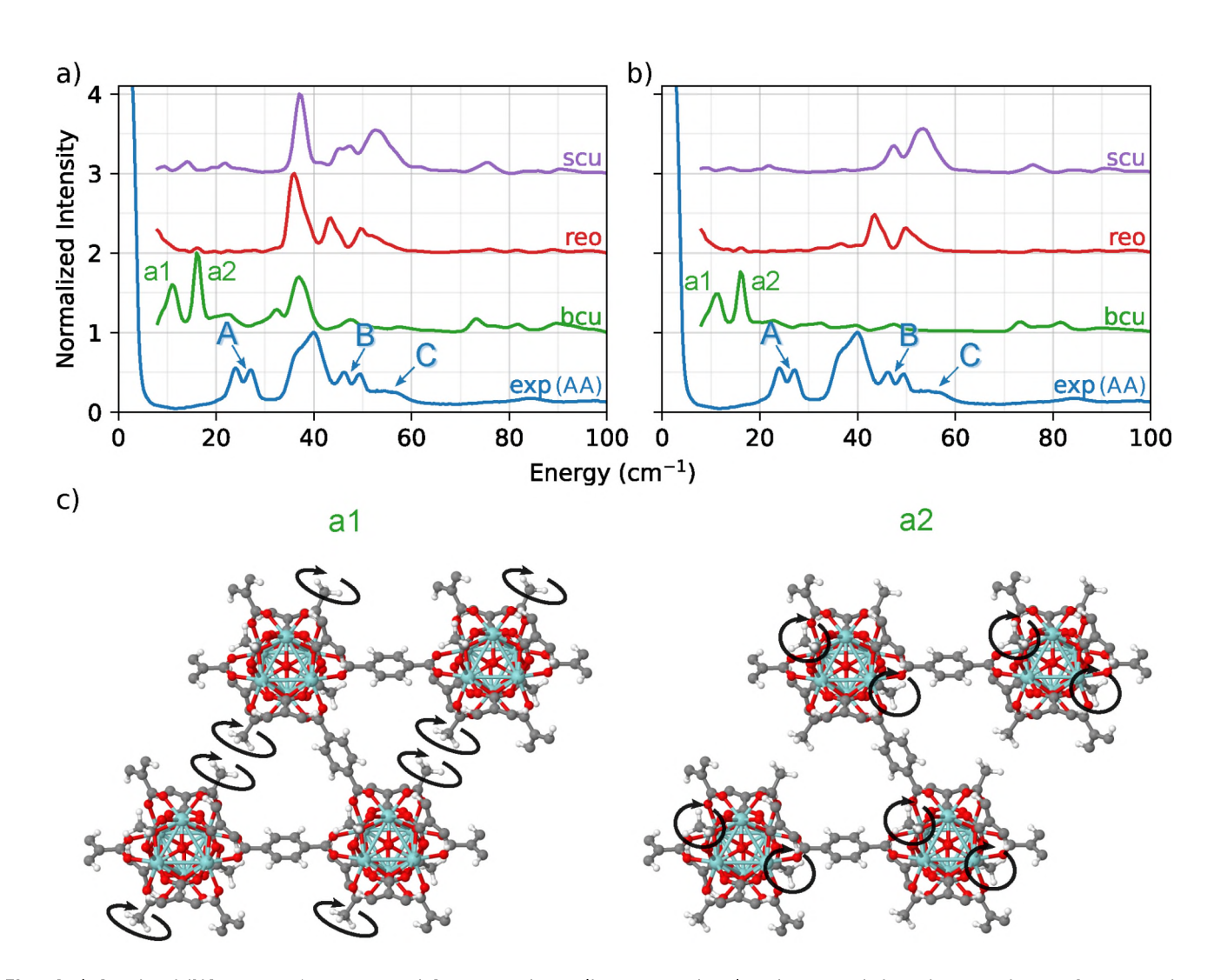


Fig. 3 a) Simulated INS spectra characterizing defective topologies (bcu, reo, and scu) with missing linkers that provide sites for acetate ligands compared to INS experimental data of UiO-66-AA. (b) INS signal contribution of only the methyl groups in the MOF compared with complete signal determined by experiment of UiO-66-AA. (c) Vibrational modes related to peaks a1 and a2 of the bcu simulation.

case that the A peaks come from coupled acetate linkers in the bcu topology, because there were no peaks with energy below 40 cm $^{-1}$  in the simulated INS spectra of the acetate defect reo and scu topologies. The B and C peaks however cannot be unambiguously assigned. Our analysis shows that the modes above 40 cm $^{-1}$  in the fingerprint region are strongly coupled with the linker and the Zr<sub>6</sub>O<sub>8</sub> node, but it is not unambiguous which acetate/linker geometry causes the doublet at B and the shoulder at C.

#### 2.3 Effect of defect symmetry

To address this issue, we focus on the bcu topology because it has the smallest unit cell, it has the same number of nodes as the fcu structure, and it provides a better fit to the full INS simulation in Figure 1 than either the reo or scu topologies. Indeed, the bcu topology can be considered as a defective fcu topology with four missing linkers per node. We consider four different variations of the bcu topology to demonstrate the structure sensitivity of the DFT-INS approach (Figure 4a). The four open missing linker sites on the bcu topology (i.e., missing linkers compared to fcu) can be occupied by either formate or acetate ligands. The simulated INS spectrum with all formate ligands (bcu-4F) was presented in Figure 1 and reproduced here (orange). The simulated INS spectrum with all acetate ligands (bcu-4A) was depicted in Figure 3 and reproduced here (green). Since the <sup>1</sup>H NMR data characterizing digested UiO-66-AA indicates the presence of both formate and acetate ligands on the node defect sites <sup>37</sup>, we next consider the possibility that the four missing linker sites in the bcu topology were occupied by two acetate and two formate ligands. When the acetate groups are oriented diagonally with each other (bcu-2A2F, red spectrum in Figure 4b), we observe a single peak at  $25~{\rm cm}^{-1}$  at the correct energy for and A peak and a single peak at 52 cm<sup>-1</sup>, which is the correct energy for a B peak. In Figure 4c, we present the mode corresponding to the peak at 25 cm<sup>-1</sup> which consists of localized rotations of the acetate groups. The peak at 52 cm<sup>-1</sup> includes significant contributions from the MOF linkers and involves coupled rocking motions of the acetate groups with the whole framework. The modes are also presented as animations bcu-2A2F\_a.gif and bcu-2A2F\_b.gif in the Supporting Information). The absence of the doublet (similar to peaks A and B in the experimental spectrum) arises because of the presence of a single diagonally opposite pair of acetate groups bound to the  $Zr_6O_6$  node. The comparison suggests that the diagonal location of the acetate group results in vibrational motions at the correct frequencies, but the simple unit cell does not represent the heterogeneity of the environment surrounding the acetate in the measured sample.

To probe a greater degree of structural complexity, we simulated a 2x1x1 unit cell of the bcu topology with diagonal defects on one node and off-diagonal defects on the other (bcu-2A2F-2F2A, purple spectrum in Figure 4). The simulated INS spectrum shows a doublet at  $48~\rm cm^{-1}$  and  $52~\rm cm^{-1}$  along with a broader peak centered at  $60~\rm cm^{-1}$ . The measured spectrum has a nearly identical doublet for the measured b1 and b2 peaks at  $46~\rm cm^{-1}$  and  $50~\rm cm^{-1}$  and the shoulder C peak is at  $55~\rm cm^{-1}$ . The slight offsets in the peak positions likely arise from the differences in

the lattice constants of the computational model and the experimental sample. The motions corresponding to the doublet b involve coupled vibrations to the framework of neighboring acetate groups whereby one acetate rotates and the other rocks (b1), and vice versa (b2). Moreover, peak c is related to vibrations of all acetate groups from both the diagonals coupled to the framework (see the animations bcu-2A2F-2F2A\_b1.gif, bcu-2A2F-2F2A\_b2.gif, and bcu-2A2F-2F2A\_c.gif in the Supporting Information). These results provide strong evidence that the experimental UiO-66-AA contains domains of the bcu-2A2F-2F2A defect structure that span multiple unit cells. Although the reo and scu topologies capped with acetates are able to reproduce peaks in the region of double peak b and shoulder c (see Figure 3), the INS simulation of the bcu-2A2F-2F2A defect structure is a much closer match to the experimental data.

In summary, the investigated sample, UiO-66-AA, has Zr-oxide nodes that have 12 possible linker attachment sites. The sample was prepared with adventitious node ligand acetic acid that occupies on average 1 of the 12 attachment sites. Formic acid was a second adventitious node ligand that was accidentally introduced during synthesis. We first simulated all four of the known UiO-66 topologies (fcu, bcu, reo, scu) and compared them to the measured INS spectrum. The fcu produced the best fit across the full energy range, which tells us that the majority of the volume 75% is a defect free fcu topology. We also showed that a series of INS peaks below 100 cm<sup>-1</sup> (labeled A, B and C) serve as fingerprint spectra for the acetic acid defect site. Next we simulated the bcu, reo, and scu topologies with all missing linker sites filled with acetic acid. Only the fully substituted bcu topology reproduced the A-peaks matching the doublet at 25 cm<sup>-1</sup> which comes from a twisting motion of the acetic acid defect. The higher energy B and C peaks couple rocking motions of the acetic acid methyl group to twisting of the linkers, but none of the fully substituted acetic acid spectra matched the measured data, indicating again that the reo and scu topologies were not present in the measured sample. Finally, we simulated the bcu topology with combined acetic acid and formic acid defects. Only geometries with acetic acid on opposite sides of the node and alternating orientation between neighboring nodes accurately reproduced the B-peak doublet and C-shoulder from the measured INS spectrum. We can therefore assign that 75% of the volume was the fcu topology with no defects. We assume, based on excellent previous work, <sup>33</sup> that the different topologies phase separate into domains. The remaining 25% of the volume seems to be roughly equally divided between the bcu topology with 100% of the adventitious node site occupied by acetic acid and the bcu topology with a 1:1 mixture of acetic acid and formic acid on the adventitious node sites. In the very roughly 12.5% of the volume with mixed acetic acid and formic acid, the sites ligands assume ordered arrangements, including occupying the opposite sides of the node and with alternating orientation between neighboring nodes. While our conclusions are consistent with a previous study by Liu et al. 34, the INS/DFT approach provides detailed structural insights (e.g., relative positions and number of acetate ligands) that are not possible with microscopy-based techniques.

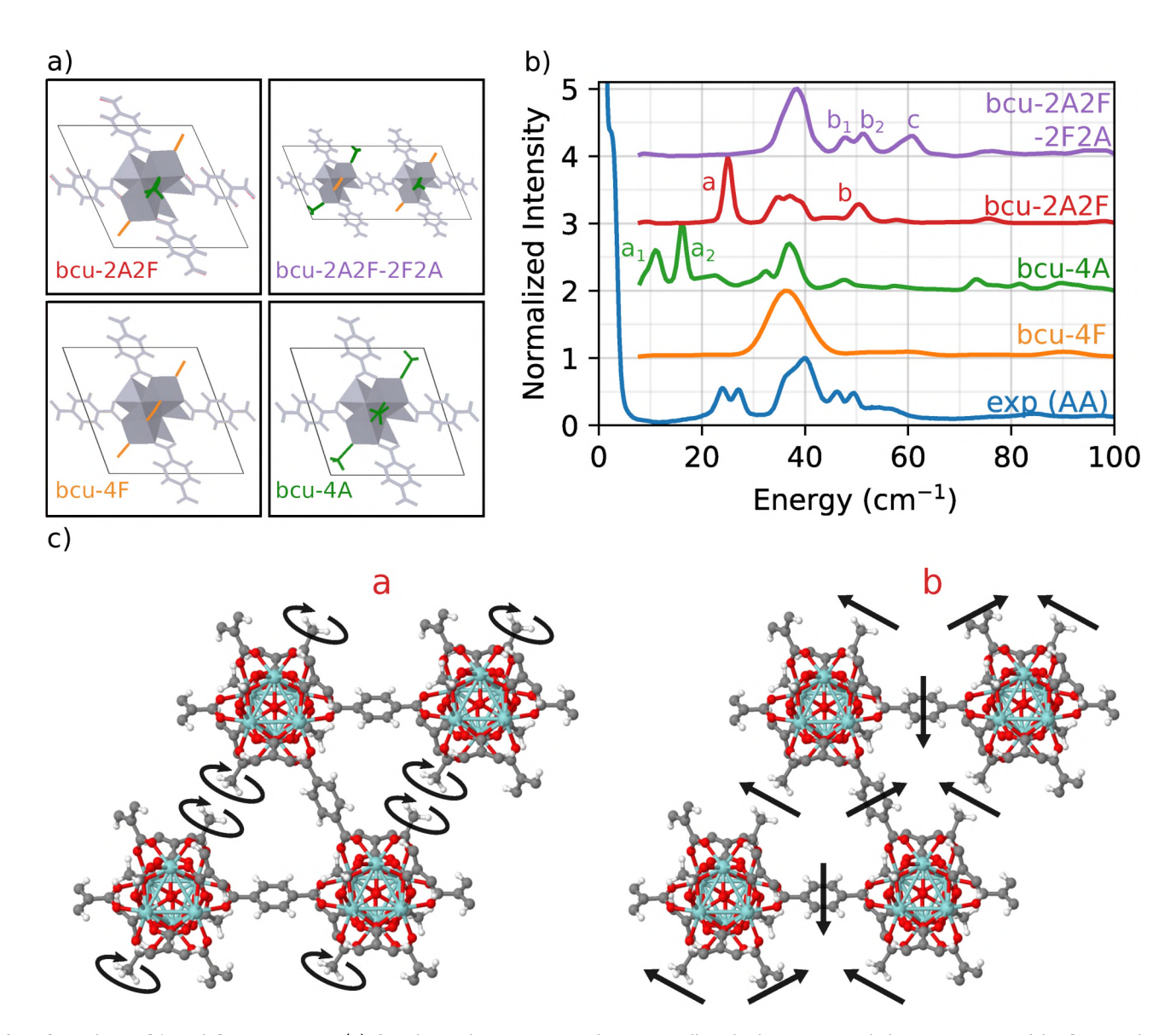


**Fig. 4** Analysis of bcu defect positions. (a) Simulation box containing bcu unit cell with the 4 missing linker sites occupied by formate ligands (bcu-4F), all 4 occupied by acetate ligands (bcu-4A), two formate groups and two acetate groups in a diagonal fashion (bcu-2A2F), and a 2x1x1 supercell with diagonal and off-diagonal defects (bcu-2A2F-2F2A). (b) Comparison of experimental INS spectra of UiO-66-AA up to 100 cm<sup>-1</sup> with simulation of bcu UiO-66 MOF with various proposed defect configurations. (c) Vibrational modes related to peaks a and b of the simulation of bcu with diagonal defects (bcu-2A2F).

# 3 Conclusions

We present a combined INS spectroscopic and simulation investigation of UiO-66 to characterize the geometry of adventitious defect sites occupied by ligands such as acetate and formate. INS spectroscopy is highly sensitive to the vibrational motions of linker molecules and defect species on MOF node defect sites because of the high resolution at low energies. Vibrations in the <100 cm<sup>-1</sup> range include subtle wag and twist motions that capture details of the molecular environment around the defect site, in this case coupling between wag motions by the methyl group on the acetate with twist motions on the terepthalic acid linker. We show a near quantitative match between the experimental INS spectrum and DFT simulated INS spectra, which demonstrates that this combination of experiment and theory is well-suited to characterization of heterogeneous reactive sites in MOFs. We suggest that this methodology should become part of the standard protocol for characterization of MOF structures. 58

# Acknowledgement

This research was supported by the Department of Energy, Basic Energy Sciences, Award DE-SC0010419, including salary for L.S.R.C., M.A.D. and A.J.M. T.S. and A.K. acknowledge partial support from NSF # 2048260. D.Y. and B.C.G. acknowledge support as part of the Inorganometallic Catalyst Design Center, an Energy Frontier Research Center funded by the U.S. Department of Energy (DOE), Office of Science, Basic Energy Sciences (DE-SC0012702). This research used resources of the National Energy Research Scientific Computing Center (NERSC), a DOE Office of Science User Facility supported by the Office of Science of the U.S. Department of Energy under Contract No. DE-AC02-05CH11231. The INS spectrum was measured at the Spallation Neutron Source, a DOE Office of Science User Facility operated by the Oak Ridge National Laboratory, partly supported by LLNL under Contract DE-AC52-07NA27344.

# Conflicts of interest

There are no conflicts to declare.

### Notes and references

- 1 H. Furukawa, F. Gándara, Y. B. Zhang, J. Jiang, W. L. Queen, M. R. Hudson and O. M. Yaghi, *Journal of the American Chemical Society*, 2014, 136, 4369–4381.
- 2 G. Rim, F. Kong, M. Song, C. Rosu, P. Priyadarshini, R. P. Lively and C. W. Jones, JACS Au, 2022, 2, 380–393.
- 3 B. Bueken, N. Van Velthoven, A. Krajnc, S. Smolders, F. Taulelle, C. Mellot-Draznieks, G. Mali, T. D. Bennett and D. De Vos, *Chemistry of Materials*, 2017, 29, 10478–10486.
- 4 Z. Fang, B. Bueken, D. E. De Vos and R. A. Fischer, Angewandte Chemie International Edition, 2015, 54, 7234–7254.
- 5 D. S. Sholl and R. P. Lively, Journal of Physical Chemistry Letters, 2015, 6, 3437–3444.
- 6 S. Dissegna, K. Epp, W. R. Heinz, G. Kieslich and R. A. Fischer, *Advanced Materials*, 2018, **30**, 1704501.
- 7 Y. Feng, Q. Chen, M. Jiang and J. Yao, Industrial and Engineering Chemistry Research, 2019, 58, 17646–17659.
- 8 X. Ma, L. Wang, Q. Zhang and H.-L. Jiang, Angewandte Chemie International Edition, 2019, 58, 12175–12179.
- 9 A. E. Baumann, D. A. Burns, B. Liu and V. S. Thoi, Communications Chemistry 2019 2:1, 2019, 2, 1–14.
- 10 A. E. Baumann, D. A. Burns, J. C. Díaz and V. S. Thoi, ACS Applied Materials & Interfaces, 2019, 11, 2159–2167.
- 11 Y. Cao, X. Mi, X. Li and B. Wang, Frontiers in Chemistry, 2021, 9, 673738.
- 12 N. Ferhi, B. Desalegn Assresahegn, C. Ardila-Suarez, N. Dissem, D. Guay and A. Duong, ACS Applied Energy Materials, 2022, 5, 1235–1243.

- 13 J. Morales-Vidal, R. García-Muelas and M. A. Ortuño, Catal. Sci. Technol., 2021, 11, 1443–1450.
- 14 Z.-D. Wang, Y. Zang, Z.-J. Liu, P. Peng, R. Wang and S.-Q. Zang, Applied Catalysis B: Environmental, 2021, 288, 119941.
- 15 T. D. Bennett, A. K. Cheetham, A. H. Fuchs and F.-X. Coudert, *Nature Chemistry* 2016 9:1, 2016, 9, 11–16.
- A. K. Cheetham, T. D. Bennett, F.-X. Coudert and A. L. Goodwin, *Dalton Trans.*, 2016, 45, 4113–4126.
- 17 B. Zheng, F. Fu, L. L. Wang, J. Wang, L. Du and H. Du, *The Journal of Physical Chemistry C*, 2018, **122**, 4300–4306.
- 18 J. Y. Choi and J. Park, ACS Applied Electronic Materials, 2021, 3, 4197-4202.
- 19 A. A. Talin, A. Centrone, A. C. Ford, M. E. Foster, V. Stavila, P. Haney, R. A. Kinney, V. Szalai, F. E. Gabaly, H. P. Yoon, F. Léonard and M. D. Allendorf, Science, 2014, 343, 66–69.
- 20 O. Basu, S. Mukhopadhyay, S. Laha and S. K. Das, Chemistry of Materials, 2022, 34, 6734–6743.
- 21 M. Islamov, H. Babaei and C. E. Wilmer, ACS Applied Materials & Interfaces, 2020, 12, 56172–56177.
- 22 H. S. Jena, A. M. Kaczmarek, C. Krishnaraj, X. Feng, K. Vijayvergia, H. Yildirim, S.-N. Zhao, R. Van Deun and P. V. Der Voort, *Crystal Growth & Design*, 2019, 19, 6339–6350.
- 23 M. Taddei, G. M. Schukraft, M. E. A. Warwick, D. Tiana, M. J. McPherson, D. R. Jones and C. Petit, J. Mater. Chem. A, 2019, 7, 23781–23786.
- 24 L. Xin, Z. Fan, G. Li, M. Zhang, Y. Han, J. Wang, K. P. Ong, L. Qin, Y. Zheng and X. Lou, New J. Chem., 2017, 41, 151–159.
- 25 G. Lorusso, E. Natividad, M. Evangelisti and O. Roubeau, Mater. Horiz., 2019, 6, 144–154.
- 26 Y. Wu, T. Binford, J. A. Hill, S. Shaker, J. Wang and A. K. Cheetham, *Chem. Commun.*, 2018, **54**, 3751–3754.
- 27 G. Zhu, Y. Liu, L. Flores, Z. R. Lee, C. W. Jones, D. A. Dixon, D. S. Sholl and R. P. Lively, *Chemistry of Materials*, 2018, 30, 262–272.
- 28 M. Rimoldi, A. J. Howarth, M. R. DeStefano, L. Lin, S. Goswami, . P. Li, J. T. Hupp and O. K. Farha, ACS Catalysis, 2017, 7, 997–1014.
- 29 D. Yang, M. A. Ortuño, V. Bernales, C. J. Cramer, L. Gagliardi and B. C. Gates, Journal of the American Chemical Society, 2018, 140, 3751–3759.
- 30 V. Bernales, D. Yang, J. Yu, G. Gümüşlü, C. J. Cramer, B. C. Gates and L. Gagliardi, ACS Applied Materials & Interfaces, 2017, 9, 33511–33520.
- 31 D. Yang, S. O. Odoh, J. Borycz, T. C. Wang, O. K. Farha, J. T. Hupp, C. J. Cramer, L. Gagliardi and B. C. Gates, ACS Catalysis, 2016, 6, 235–247.
- 32 F. E. Chen, T. A. Pitt, D. J. Okong'o, L. G. Wetherbee, J. J. Fuentes-Rivera and P. J. Milner, Chemistry of Materials, 2022, 34, 3383–3394.
- 33 M. J. Cliffe, W. Wan, X. Zou, P. A. Chater, A. K. Kleppe, M. G. Tucker, H. Wilhelm, N. P. Funnell, F. X. Coudert and A. L. Goodwin, *Nature Communications*, 2014, 5, 1–8.
- 34 L. Liu, Z. Chen, J. Wang, D. Zhang, Y. Zhu, S. Ling, K. W. Huang, Y. Belmabkhout, K. Adil, Y. Zhang, B. Slater, M. Eddaoudi and Y. Han, *Nature Chemistry*, 2019, 11, 622–628.
- 35 H. Wu, T. Yildirim and W. Zhou, Journal of Physical Chemistry Letters, 2013, 4, 925–930.
- 36 R. C. Klet, Y. Liu, T. C. Wang, J. T. Hupp and O. K. Farha, *Journal of Materials Chemistry A*, 2016, 4, 1479–1485.
- 37 R. Wei, C. A. Gaggioli, G. Li, T. Islamoglu, Z. Zhang, P. Yu, O. K. Farha, C. J. Cramer, L. Gagliardi, D. Yang and B. C. Gates, *Chemistry of Materials*, 2019, 31, 1655–1663.
- 38 T. F. Harrelson, V. Dantanarayana, X. Xie, C. Koshnick, D. Nai, R. Fair, S. A. Nuñez, A. K. Thomas, T. L. Murrey, M. A. Hickner, J. K. Grey, J. E. Anthony, E. D. Gomez, A. Troisi, R. Faller and A. J. Moulé, *Materials Horizons*, 2019, 6, 182–191.
- 39 T. F. Harrelson, Y. Q. Cheng, J. Li, I. E. Jacobs, A. J. Ramirez-Cuesta, R. Faller and A. J. Moulé, Macromolecules, 2017, 50, 2424–2435.
- 40 C. H. . Philip, S. F. Parker, A. J. Ramirez-Cuesta and J. Tomkinson, Vibrational spectroscopy with neutrons: With applications in chemistry, biology, materials science and catalysis, World Scientific Publishing Co., 2005, pp. 1–642.
- 41 M. E. Casco, J. Fernández-Catalá, Y. Cheng, L. Daemen, A. J. Ramirez-Cuesta, C. Cuadrado-Collados, J. Silvestre-Albero and E. V. Ramos-Fernandez, *ChemistrySelect*, 2017, 2, 2750–2753.
- 42 A. Deacon, L. Briquet, M. Malankowska, F. Massingberd-Mundy, S. Rudić, T. l. Hyde, H. Cavaye, J. Coronas, S. Poulston and T. Johnson, *Communications Chemistry* 2022 5:1, 2022, 5, 1–10.
- 43 D. Vong, T. Nematiaram, M. A. Dettmann, T. L. Murrey, L. S. R. Cavalcante, S. M. Gurses, D. Radhakrishnan, L. L. Daemen, J. E. Anthony, K. J. Koski, C. X. Kronawitter, A. Troisi and A. J. Moulé, *The Journal of Physical Chemistry Letters*, 2022, 13, 5530–5537.
- 44 L. Valenzano, B. Civalleri, S. Chavan, S. Bordiga, M. H. Nilsen, S. Jakobsen, K. P. Lillerud and C. Lamberti, *Chemistry of Materials*, 2011, **23**, 1700–1718.
- 45 H. Wu, Y. S. Chua, V. Krungleviciute, M. Tyagi, P. Chen, T. Yildirim and W. Zhou, Journal of the American Chemical Society, 2013, 135, 10525–10532.
- 46 S. Øien, D. Wragg, H. Reinsch, S. Svelle, S. Bordiga, C. Lamberti and K. P. Lillerud, Crystal Growth & Design, 2014, 14, 5370–5372.
- 47 M. Vandichel, J. Hajek, F. Vermoortele, M. Waroquier, D. E. D. Vos and V. V. Speybroeck, CrystEngComm, 2014, 17, 395–406.
- 48 T. D. Bennett, T. K. Todorova, E. F. Baxter, D. G. Reid, C. Gervais, B. Bueken,

- B. Van De Voorde, D. De Vos, D. A. Keen and C. Mellot-Draznieks, Physical Chem $istry\ Chemical\ Physics,\ 2016,\ \textbf{18},\ 2192-2201.$
- F. Zhou, N. Lu, B. Fan, H. Wang and R. Li, Journal of Energy Chemistry, 2016, 5,
- 50 C. Atzori, G. C. Shearer, L. Maschio, B. Civalleri, F. Bonino, C. Lamberti, S. Svelle, K. P. Lillerud and S. Bordiga, Journal of Physical Chemistry C, 2017, 121, 9312– 9324.
- 51 D. N. Johnstone, F. C. N. Firth, C. P. Grey, P. A. Midgley, M. J. Cliffe and S. M. Collins, Journal of the American Chemical Society, 2020, 142, 13081–13089.
- 52 K. Tan, H. Pandey, H. Wang, E. Velasco, K. Y. Wang, H. C. Zhou, J. Li and T. Thonhauser, Journal of the American Chemical Society, 2021, 143, 6328-6332.
- Y. Q. Cheng, L. L. Daemen, A. I. Kolesnikov and A. J. Ramirez-Cuesta, *Journal of Chemical Theory and Computation*, 2019, **15**, 1974–1982.
- 54 M. A. Dettmann, L. S. Cavalcante, C. Magdaleno, K. Masalkovaitė, D. Vong, J. T. Dull, B. P. Rand, L. L. Daemen, N. Goldman, R. Faller and A. J. Moulé, *Journal of Chemical Theory and Computation*, 2021, **17**, 7313–7320.
- 55 L. S. Cavalcante, L. L. Daemen, N. Goldman and A. J. Moulé, Journal of Chemical Information and Modeling, 2021, 61, 4486-4496.
- 56 A. Togo and I. Tanaka, Scripta Materialia, 2015, 108, 1-5.
- 57 M. E. Casco, Y. Q. Cheng, L. L. Daemen, D. Fairen-Jimenez, E. V. Ramos-Ferná Ndez, A. J. Ramirez-Cuesta and J. Silvestre-Albero, Chem. Commun, 2016, 52, 3639.
- 58 C. Gropp, S. Canossa, S. Wuttke, F. Gándara, Q. Li, L. Gagliardi and O. M. Yaghi, ACS Central Science, 2020, 6, 1255-1273.